



# Cross-scale Dynamics Driven by Plasma Jet Braking in Space

C. M. Liu<sup>1,2,3</sup> , A. Vaivads<sup>3</sup>, Y. V. Khotyaintsev<sup>2</sup> , H. S. Fu<sup>1</sup> , D. B. Graham<sup>2</sup> , K. Steinvall<sup>2,4</sup>, Y. Y. Liu<sup>1</sup> , and J. L. Burch<sup>5</sup>

<sup>1</sup> School of Space and Environment, Beihang University, Beijing, People's Republic of China

<sup>2</sup> Swedish Institute of Space Physics, Uppsala, Sweden

<sup>3</sup> Space and Plasma Physics, KTH Royal Institute of Technology, Stockholm, Sweden

<sup>4</sup> Space and Plasma Physics, Department of Physics and Astronomy, Uppsala University, Uppsala, Sweden

<sup>5</sup> Southwest Research Institute, San Antonio, TX, USA

Received 2021 March 1; revised 2021 December 25; accepted 2022 January 7; published 2022 February 24

## Abstract

Plasma jets are ubiquitous in space. In geospace, jets can be generated by magnetic reconnection. These reconnection jets, typically at fluid scale, brake in the near-Earth region, dissipate their energies, and drive plasma dynamics at kinetic scales, generating field-aligned currents that are crucial to magnetospheric dynamics. Understanding of the cross-scale dynamics is fundamentally important, but observation of coupling among phenomena at various scales is highly challenging. Here we report, using unprecedentedly high-cadence data from NASA's Magnetospheric Multiscale Mission, the first observation of cross-scale dynamics driven by jet braking in geospace. We find that jet braking causes MHD-scale distortion of magnetic field lines and development of an ion-scale jet front that hosts strong Hall electric fields. Parallel electric fields arising from the ion-scale Hall potential generate intense electron-scale field-aligned currents, which drive strong Debye-scale turbulence. Debye-scale waves conversely limit intensity of the field-aligned currents, thereby coupling back to the large-scale dynamics. Our study can help in understanding how energy deposited in large-scale structures is transferred into small-scale structures in space.

*Unified Astronomy Thesaurus concepts:* Solar magnetic reconnection (1504); Space plasmas (1544)

## 1. Introduction

Plasma jets, which are high-speed plasma flows, are ubiquitous in space. Jets, carrying massive moment and energy, are dynamic regions hosting intense plasma activities, such as energy conversion (e.g., Huang et al. 2012, 2015a; Fu et al. 2017; Yao et al. 2017), wave-particle interactions (e.g., Khotyaintsev et al. 2011; Hwang et al. 2014; Zhou et al. 2014; Huang et al. 2015b, 2019; Jiang et al. 2020; Wei et al. 2021, 2022), and particle acceleration (e.g., Fu et al. 2011, 2013, 2014; Lu et al. 2016; Liu & Fu 2019; Huang et al. 2020; Liu et al. 2020), all of which are crucial in space plasma environments. In geospace, jets are usually generated by magnetic reconnection—a process converting magnetic field energy into particle thermal and kinetic energy (e.g., Vaivads et al. 2004; Torbert et al. 2018). Dynamics of these reconnection jets typically at large scale is controlled by their interactions with the ambient plasma, which will dissipate and redistribute jet kinetic energy by thermalization and diversion (e.g., Khotyaintsev et al. 2011; Angelopoulos et al. 2013; Liu et al. 2019), usually through a kinetic-scale plasma boundary commonly referred to as jet front (e.g., Runov et al. 2009; Fu et al. 2012a, 2012b; Liu et al. 2018a, 2018b). When jets propagate toward the near-Earth region ( $\sim 9$ – $14 R_E$ , where  $R_E$  is the Earth radius), they are gradually slowed down and get diverted due to processes at different scales, a process known as jet braking (e.g., Shiokawa et al. 1997; Ohtani et al. 2004; Sergeev et al. 2009; Drake et al. 2014; Nakamura et al. 2018).

Jet braking, usually occurring at global scale, is of great significance to the planets' magnetospheric dynamics. In

geospace, it is associated with many important large-scale magnetospheric phenomena, such as magnetic field dipolarization (e.g., Birn et al. 2013) and energetic particle injections (e.g., Deng et al. 2010; Zhou et al. 2013, 2018; Grigorenko et al. 2016; Turner et al. 2016; Fu et al. 2020). It also induces plasma activities at kinetic scales, such as wave-particle interaction (e.g., Ergun et al. 2014) and formation of field-aligned current (e.g., Liu et al. 2013)—the bridge coupling the magnetosphere with the ionosphere. Jet braking, together with the associated magnetospheric dynamics at various scales, contributes to the most violent energy release in geospace, the auroral substorm (Akasofu 2015). The multiscale dynamics in association with jet braking is thus fundamentally important in space physics. However, how processes at different scales couple among each other and how cross-scale dynamics modulate the magnetosphere-ionosphere coupling remain hitherto unknown.

Understanding of the cross-scale dynamics in space is crucial, but observation of coupling among phenomena at various scales is highly challenging. To observe dynamics at various scales in space, multipoint spacecraft measurements at sufficiently high cadence are usually required. The advent of NASA's recently launched Magnetospheric Multiscale (MMS) mission consisting of four identical satellites deployed in a tetrahedron configuration at electron scale (Burch et al. 2016), which measure particle 3D velocity distributions orders of magnitude faster than previous spacecraft, provides a unique opportunity to study cross-scale dynamics in geospace.

Here using unprecedentedly high-cadence data from the MMS mission, we report on the first observation of cross-scale dynamics driven by jet braking in geospace. We observe plasma dynamics developing from MHD and down to Debye scales during jet braking, and determine the associated plasma



Original content from this work may be used under the terms of the [Creative Commons Attribution 4.0 licence](https://creativecommons.org/licenses/by/4.0/). Any further distribution of this work must maintain attribution to the author(s) and the title of the work, journal citation and DOI.

characteristics at different scales in detail. We reveal that Debye-scale turbulence couples back to the large-scale plasma dynamics via a Buneman-type instability, establishing cross-scale physics and mediating the magnetosphere–ionosphere coupling.

## 2. Event Overview

On 2018 September 8, the four MMS spacecraft, in a tetrahedron formation separated by  $\sim 50$  km, were located in near-Earth magnetotail, at  $[-13.2, 4.5, 3.3] R_E$  in the Geocentric Solar Magnetospheric (GSM) coordinates. The time interval discussed for the event starts from 14:40:00 to 15:06:00 Universal Time (UT), when a quiescent plasma sheet was initially observed by the spacecraft, and then followed by disturbances induced by braking of a plasma jet. Data used in this study are from the fluxgate magnetometers (Russell et al. 2016), the Fast Plasma Investigation (Pollock et al. 2016), the Axial Double Probes (Ergun et al. 2014), and the Spin-plane Double Probes (Lindqvist et al. 2016). All data are presented in the GSM coordinates unless noted otherwise.

We start with presenting long-time observations to provide a general overview for the event, as shown in Figure 1. Before  $\sim 14:50:00$  UT, the spacecraft were located in the south of the current sheet ( $B_X < 0$ , Figure 1(a)) and observed a quiescent plasma sheet. Starting from 14:50:00 UT, MMS observed a high-speed ion jet with maximum speed approaching  $400 \text{ km s}^{-1}$  (Figure 1(c)), close to  $0.9 V_{\text{Alfvén}}$ , where  $V_{\text{Alfvén}}$  is the Alfvén speed, calculated based on plasma parameters in the quiet plasma sheet. The ion jet shows comparable  $V_x$  and  $V_y$  components, indicating jet diversion in the near-Earth region (Figure 1(c)). Associated with the jet, both magnetic fields and particle parameters exhibit distinct disturbances. The magnetic field  $B_X$  component dramatically decreases (Figure 1(a)), indicating spacecraft close entry into the neutral sheet. The magnetic field  $B_Y$  component, which stays positive in the quiet plasma sheet, clearly shows a bipolar variation. The magnetic field  $B_Z$  component increases sharply up to 20 nT, characterizing the main feature of jet front or dipolarization front. Along with the magnetic field disturbances, plasma density begins with a steady increase (Figure 1(b)), indicating compression of local plasma, then decreases sharply across the front, maintaining local pressure balance. Meanwhile, electron and ion energies gradually drop (Figures 1(d)–(e)). Behind the front, jet starts to rebound, manifested by the damped oscillations of the  $V_x$  and  $V_y$  components (e.g., Panov et al. 2010). The magnetic field and particle energy also fluctuate, showing multiple regions hosting local dipolarization and particle acceleration. The overview demonstrates that the MHD-scale plasma jet brakes and gets diverted in the near-Earth region, giving rise to distinct disturbances of both magnetic fields and particles at various scales therein.

## 3. MHD Scale: Distortion of Magnetic Field Lines

We now focus on the disturbances of the magnetic field associated with jet braking. We zoom into the region where magnetic fields experience a large change, as shown in Figures 1(f)–(j). We observe that prior to the sharp dipolarization, the magnetic field  $B_Z$  component, which stays positive in the quiet plasma sheet, starts to decrease at  $\sim 14:51:23$  UT, becomes negative, and then recovers as positive. The dominant  $B_Y$  component shows more distinct variation: it starts to

increase from  $\sim 14:51:22.0$  UT, peaks at  $\sim 11$  nT at  $\sim 14:51:25.5$  UT, reverses sign near  $14:51:26.8$  UT, reaches a negative peak ( $\sim -20$  nT) at  $\sim 14:51:30.1$  UT, and then drops sharply at the front. The bipolar change of the  $B_Y$  component at  $\sim 14:51:26.8$  UT is of particular interest and associated with the reversal of the  $B_X$  component (from negative to positive) at the same time, indicating that the  $B_Y$  variation corresponds to a spacecraft crossing of the neutral sheet from the southern hemisphere into northern hemisphere.

The change in magnetic fields described above, particularly the  $B_Y$  variation, may result from distortion of the magnetic field lines driven by the jet diversion. Recent MHD simulations (e.g., Birn & Hesse 2014; Merkin et al. 2019) show that during jet braking, an azimuthally diverted jet can lead to distortion of nearby magnetic field lines, consequently enhancing  $|B_Y|$  away from the neutral sheet center. An important feature associated with such distortion is that  $B_Y$  reverses sign when crossing the current sheet (see Figure 10 in Birn & Hesse 2014), as observed in our event. In panel (i) we see that the jet is deflected into the  $+Y$  direction; thus, the magnetic field lines will consequently be distorted into the  $+Y$  direction, leading to increase of  $|B_Y|$  at both hemispheres (positive  $B_Y$  in the south but negative  $B_Y$  in the north). When MMS spacecraft cross the neutral sheet from the southern into the northern hemisphere, bipolar change of  $B_Y$  from positive to negative thus will be observed, consistent with our observations (Figure 1(g)). In addition, the MHD simulations (Birn & Hesse 2014) suggest that decrease of  $|B_X|$  away from the neutral sheet and local reduction of  $B_Z$  ahead of the front, both of which are seen in our observation, are also connected with jet braking. Therefore, we conclude that the observed variation of the magnetic fields prior to the front is attributed to an MHD convection effect driven by jet diversion. Such an MHD effect is related to a local ion frozen-in condition being satisfied (not shown). Note that the magnetic field distortion is attributable to the large-scale evolution of the MHD flow and thus is not necessarily correlated with the change of ion speed at local scale, which usually involves kinetic-scale processes (the ion frozen-in condition is broken). For example, sharp changes of  $B_Y$  and  $B_X$  observed at the dipolarization front (DF) (such as  $B_X$  reversal near 14:51:31 UT and  $B_Y$  decreasing at  $\sim 14:51:32$  UT) cannot be attributed to the MHD effect (since ions are unmagnetized at the DF, see discussions below), but instead related to kinetic-scale dynamics at the DF. In particular, we observe short-period fluctuating electric fields at the front (Figure 1(j)), suggesting presence of the kinetic-scale dynamics associated with the jet braking.

## 4. Ion Scale: Tailward Hall Electric Field

We now zoom further into the front region to investigate the kinetic-scale dynamics, as shown in Figure 2. The front is characterized by an increase of  $B_Z$ , from  $\sim 14:51:30.4$  to  $\sim 14:51:31.8$  UT (Figure 2(a)). Based on timing difference among four MMS observations, we determine the propagation velocity of the front as  $230 \times [0.95, 0.28, 0.09] \text{ km s}^{-1}$ . The front thickness is estimated as 320 km,  $\sim 1 d_i$ , where  $d_i$  is the ion initial length calculated based on density observed in the quiet plasma sheet. Across the front, plasma density drops dramatically (Figure 2(b)). Intense electric fields at sub-ion scale are observed at the front, exhibiting distinct features at different subregions. For example, on the high-density side of the front, a strong earthward electric field  $+E_X$ , associated with

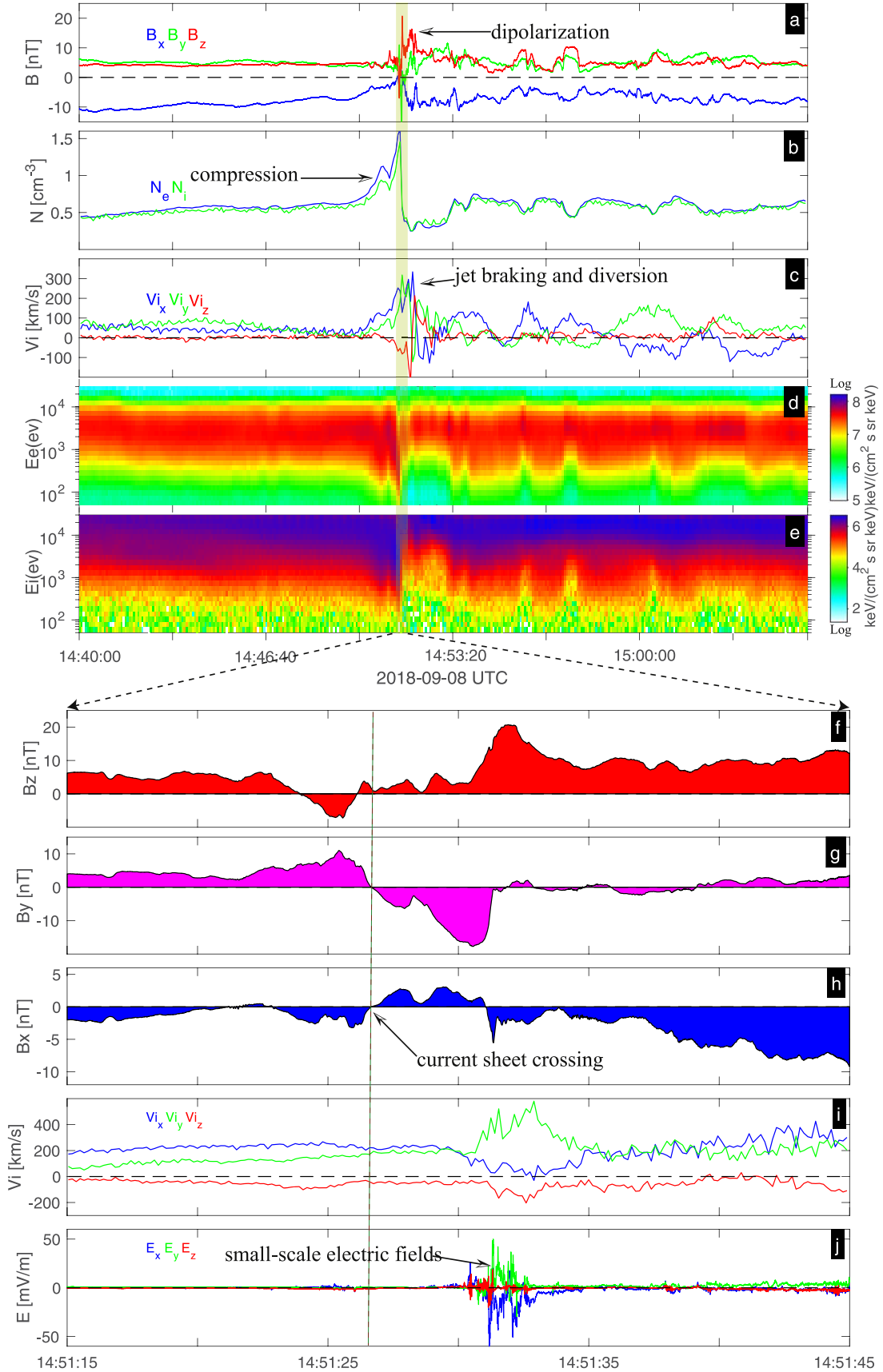


**Figure 1.** Plasma jet braking detected by MMS3 on 2018 September 8: (a) three components of the magnetic field in GSM coordinates, (b) plasma density, (c) ion bulk flow velocity, (d) electron energy spectrum, (e) ion energy spectrum, (f) the magnetic field  $B_z$  component, (g) the magnetic field  $B_y$  component, (h) the magnetic field  $B_x$  component, (i) ion bulk velocity, and (j) electric field.

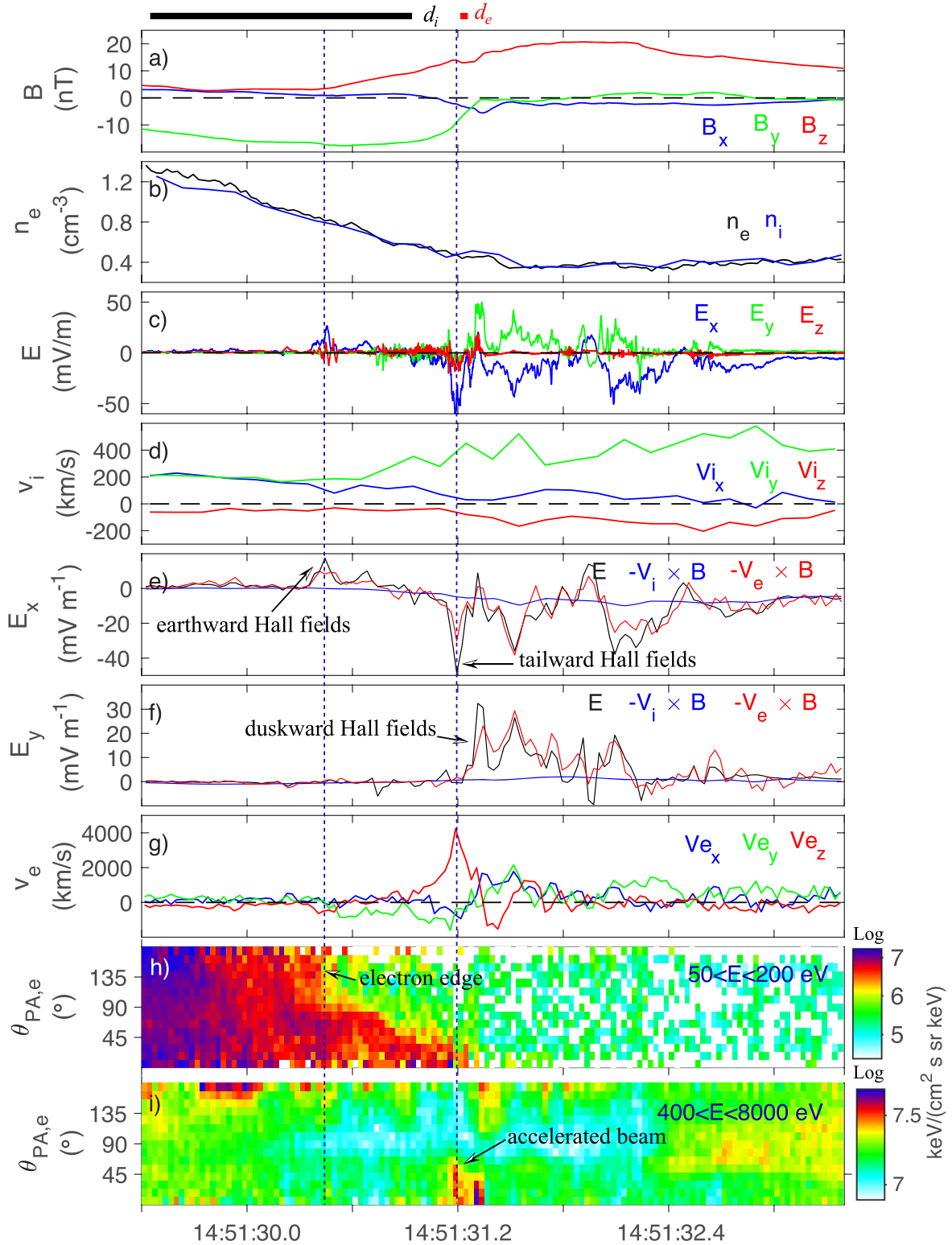


**Figure 2.** Ion-scale plasma dynamics at the DF: (a) three components of magnetic field, (b) plasma density, (c) electric field, (d) ion bulk flow velocity, (e), (f) particle convection electric fields and measured electric field, (g) electron bulk flow velocity, and (h) and (i) electron pitch angle distribution. The black and red bars on the top represent ion and electron inertial length scale, respectively.

fluctuating  $E_z$ , is observed ( $\sim 14:51:30.5$  UT; Figure 2(c)); while on the low-density side of the front, an intense tailward  $-E_x$ , along with a primarily duskward electric field  $E_y$ , is detected ( $\sim 14:51:31.2$  UT; Figure 2(c)). Compared to the earthward electric fields on the high-density side, the tailward electric fields on the low-density side are more intense and

exhibit a larger temporal scale, indicating that their formation may be quite different.

The sub-ion-scale electric fields observed on the front's low-density side—particularly the tailward electric fields—are established in response to the evolution of the jet. We compare the observed electric fields with the particle convection terms to



determine if particles are frozen-in. We find that the ion convection term clearly deviates from the observed electric fields, but the electron convection term basically follows it (Figures 2(e)–(f)). Thus, ions are demagnetized within the front, while electrons still approximately remain frozen-in, establishing Hall physics at the front, consistent with previous studies (e.g., Fu et al. 2012a; Sun et al. 2014). During the jet braking, high-speed ions behind the front catch up with the braking front and get reflected, leading to charge separation, which generates the tailward Hall fields, a scenario predicted by recent kinetic simulations of jet braking (Drake et al. 2014).

The Hall electric fields are found to be connected with electron dynamics as well. The earthward Hall electric field on the high-density side corresponds to an electron edge (Figure 2(h)), which constrains penetration of electrons at large pitch angles and permits propagation of a parallel-propagating electron beam. Such an observation suggests a possible relation between parallel electric fields and the tailward electric fields, although they have different directions (see detailed discussions below). The electron beam is further accelerated on the low-density side and forms a fast electron jet with maximum speed approaching  $5000 \text{ km s}^{-1}$ , which is observed in association with the tailward electric field (Figure 2(i)). Considering the duration of the accelerated electron beam ( $\sim 0.2 \text{ s}$ ), it has a scale of  $46 \text{ km}$ ,  $\sim 6 d_e$ , where  $d_e$  is electron initial length.

### 5. Electron Scale: Beam Formation

In order to understand formation of the electron beam, we zoom into the beam region, as shown in Figure 3. Intense field-aligned current with maximum magnitude approaching  $400 \text{ nA m}^{-2}$ , is observed along with the beam. In Figure 3(c) where electron 1D reduced velocity distributions parallel to the magnetic field is shown, we observe a cold electron beam being accelerated up to  $\sim 1.7 \times 10^4 \text{ km s}^{-1}$ ,  $\sim 0.95 V_{te}$ , where  $V_{te}$  is the electron thermal speed. Two features of the beam formation are identified: (1) the accelerated fast beam arises from a persistent slow beam; (2) the beam speed increases linearly over time, possibly indicating constant acceleration. To investigate further the beam formation, we assume the slow beam as the source of the accelerated beam, based on the following reasons: (1) jet braking causes stopping of local flux tubes at the front (local ion flow speed approaches zero,  $V_{ix} \sim 0 \text{ km s}^{-1}$ , see Figure 2(d)), such that the same flux tube is probably observed; and (2) the slow beam exhibits similar properties (density and temperature) as the accelerated beam. Using the assumed source, we can estimate the parallel potential responsible for the electron acceleration via Liouville mapping (Figures 3(d)–(e)). According to the Liouville theorem, the initial-state phase space density (PSD) and the final-state PSD are correlated by the following equation:

$$F_{\text{initial}}(E_{\text{initial}} + e\Phi_{\parallel}) = F_{\text{final}}(E_{\text{final}}) \quad (1)$$

where  $E_{\text{initial}}$ ,  $\Phi_{\parallel}$ , and  $E_{\text{final}}$  are initial energy, parallel potential, and final energy, respectively. The parallel electrostatic potential is obtained by best fitting the initial PSD to the final PSD. One can see that with  $\Phi_{\parallel} \sim 1000 \text{ V}$ , the mapped electron PSD from the source perfectly matches the observed one. Therefore, we conclude that the beam acceleration is attributed to parallel electrostatic potential, which causes the observed constant acceleration.

Based on the constant acceleration, we can also estimate the parallel electric field by assuming the observed constant acceleration as a temporal evolution, since the same flux tube is probably observed during the acceleration. Thus, the parallel electric field can be estimated as  $E_{\parallel} = \Delta V / \Delta t \times m_e / e \approx 0.8 \text{ mV m}^{-1}$ , where  $\Delta V$  is the speed increase and  $\Delta t$  is the acceleration duration obtained from a linear fitting in (Figure 3(c)). The acceleration length can be calculated as  $\Delta L = \int V \cdot dt \approx 1100 \text{ km}$ . Based on the estimated electric field and acceleration length, we can calculate the parallel electrostatic potential as  $\Delta\phi = E_{\parallel} \times \Delta L \approx 900 \text{ V}$ . The estimated potential is in excellent agreement with the result obtained from the Liouville mapping.

### 6. Debye Scale: Electrostatic Turbulence

The observed fast beam can be a free energy source for electrostatic instabilities at smaller scales. In Figure 4(c), where the parallel electric field is presented, we indeed observe strong fluctuating parallel electric fields at the front, which are well correlated with the peak of the field-aligned current. These are driven by the fast electron beam (Figure 4(b)), possibly suggesting development of current-driven electrostatic turbulence. When zooming in into the fluctuating electric fields, we find that these fields are characterized by short-period bipolar structures (Figure 4(d)), and thus we interpret them as electrostatic waves (e.g., Graham et al. 2016; Huang et al. 2016; Steinvall et al. 2019). To understand the wave properties, knowledge of wave phase speed is necessary. However, here we cannot resolve the wave speed using timing analysis because the four MMS spacecraft observe different waveforms; and we cannot perform a probe-probe interferometry method either because the wave speed is too fast to be distinguished by different probes (Steinvall et al. 2019). A rough estimate of their speed, nevertheless, can be performed by assuming that the waves have a typical peak-peak length scale of  $9 \lambda_D$ , where  $\lambda_D$  is the Debye length, as suggested by recent statistical analysis (Graham et al. 2016). Based on the observed wave peak-to-peak duration, the estimated wave speed is  $\sim 600 \text{ km s}^{-1}$ , close to the local ion thermal speed. Such speed is relatively slow, suggesting that the waves may be driven by a Buneman-type instability (Norgren et al. 2015).

To understand the relation between the waves and accelerated beam, we solve 1D electrostatic plasma dispersion relation, considering a three-component plasma that consists of one ion population and two electron populations. The dispersion equation is:

$$1 - \frac{\omega_{pi}^2}{k^2 V_i^2} Z' \left( \frac{\omega}{k V_i} \right) - \frac{\omega_{pe,bg}^2}{k^2 V_{te,bg}^2} Z' \left( \frac{\omega - k V_{bg}}{k V_{te,bg}} \right) - \frac{\omega_{pe,beam}^2}{k^2 V_{te,beam}^2} Z' \left( \frac{\omega - k V_b}{k V_{te,beam}} \right) = 0, \quad (2)$$

where  $Z$  is the plasma dispersion function,  $V_{ts} = \sqrt{2k_B T_s / m_s}$  is the thermal speed,  $\omega_{ps} = \sqrt{n_s e^2 / \epsilon_0 m_s}$  is the plasma frequency of population  $s$ , and  $V_{bg}$  and  $V_b$  are the background speed and beam speed, respectively. We fit the observed electron 1D PSD using two Maxwellian distributions to obtain the plasma parameters (Figure 4(e)):

$$f(v) = n_{e,bg} \cdot \pi^{-1/2} \cdot e^{((v-v_{bg})/V_{te,bg})^2} + n_{e,beam} \cdot \pi^{-1/2} \cdot e^{((v-v_b)/V_{te,beam})^2}. \quad (3)$$

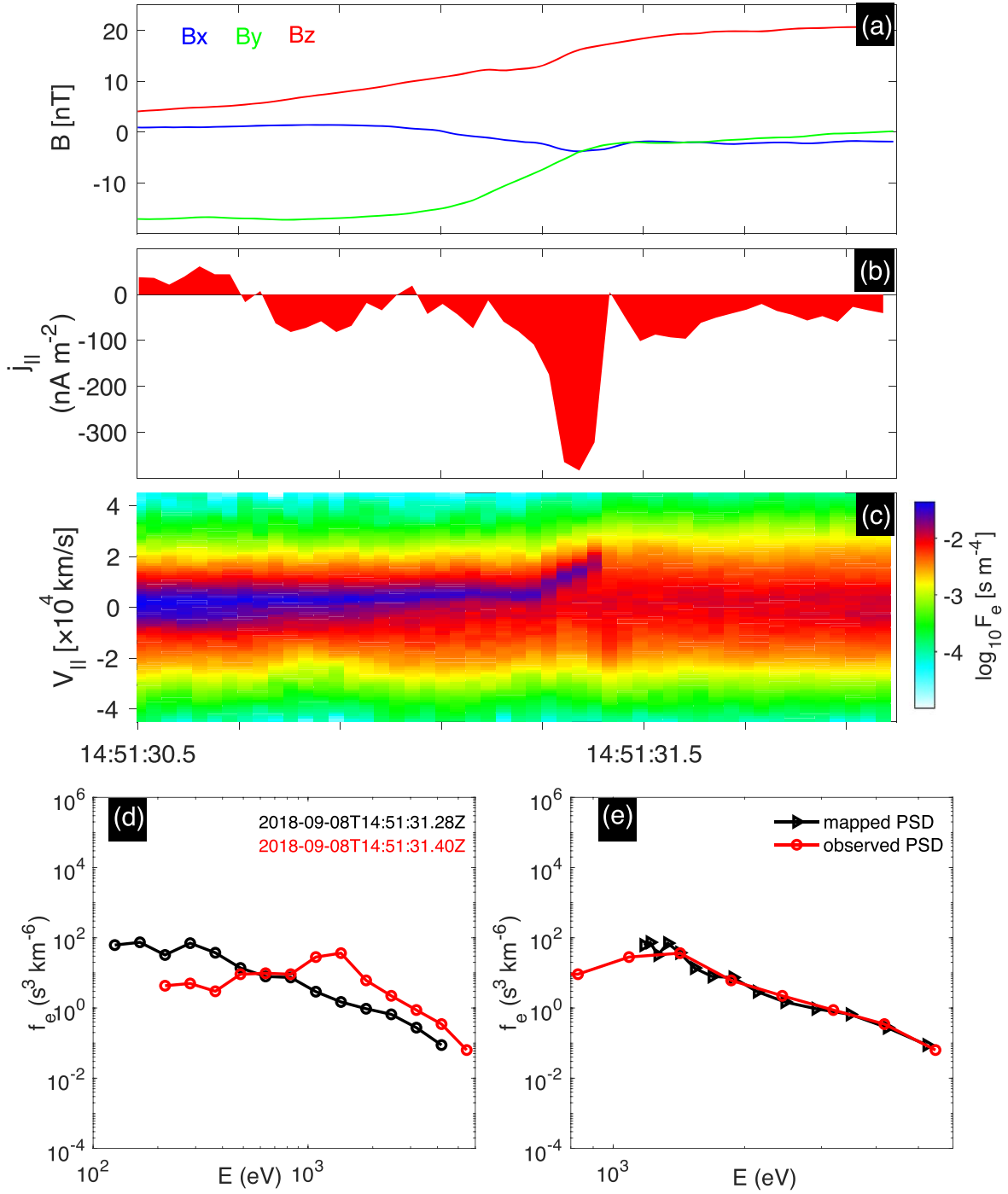


**Figure 3.** Electron-scale field-aligned currents and electron beam acceleration at the front: (a) three components of the magnetic field, (b) field-aligned currents, (c) electron 1D reduced velocity distribution, (d) electron phase space density, and (e) Liouville mapping.

The obtained parameters are:  $n_{e,bg} = 0.14 \text{ cm}^{-3}$ ,  $T_{e,bg} = 1300 \text{ eV}$ ,  $V_{e,bg} = -2400 \text{ km s}^{-1}$ ,  $n_{e,beam} = 0.1 \text{ cm}^{-3}$ ,  $T_{e,beam} = 90 \text{ eV}$ ,  $V_b = 16,500 \text{ km s}^{-1}$ , and  $T_i = 4000 \text{ eV}$ . With these parameters, the predicted properties of the unstable mode are estimated, as shown in (Figure 4(f)). One can see that the accelerated electron beam is indeed unstable, and wave frequency corresponding to a positive growth rate covers a wide range. We find that the observed wave property (frequency and wavenumber, marked by the green circle) is in agreement with the predictions, and that the predicted wave

phase speed is  $\sim 1000 \text{ km s}^{-1}$ , close to the estimated speed. Therefore, we conclude that the electrostatic waves are generated by a Buneman-type instability (e.g., Che et al. 2010; Norgren et al. 2015). Such Buneman-type waves can theoretically couple fast electrons and slow ions due to their slow phase speed and large wave potential, i.e., the slow waves can resonate with both ions and electrons through Landau resonance, leading to coupling between ions and electrons and therefore the resistivity (e.g., Norgren et al. 2015;

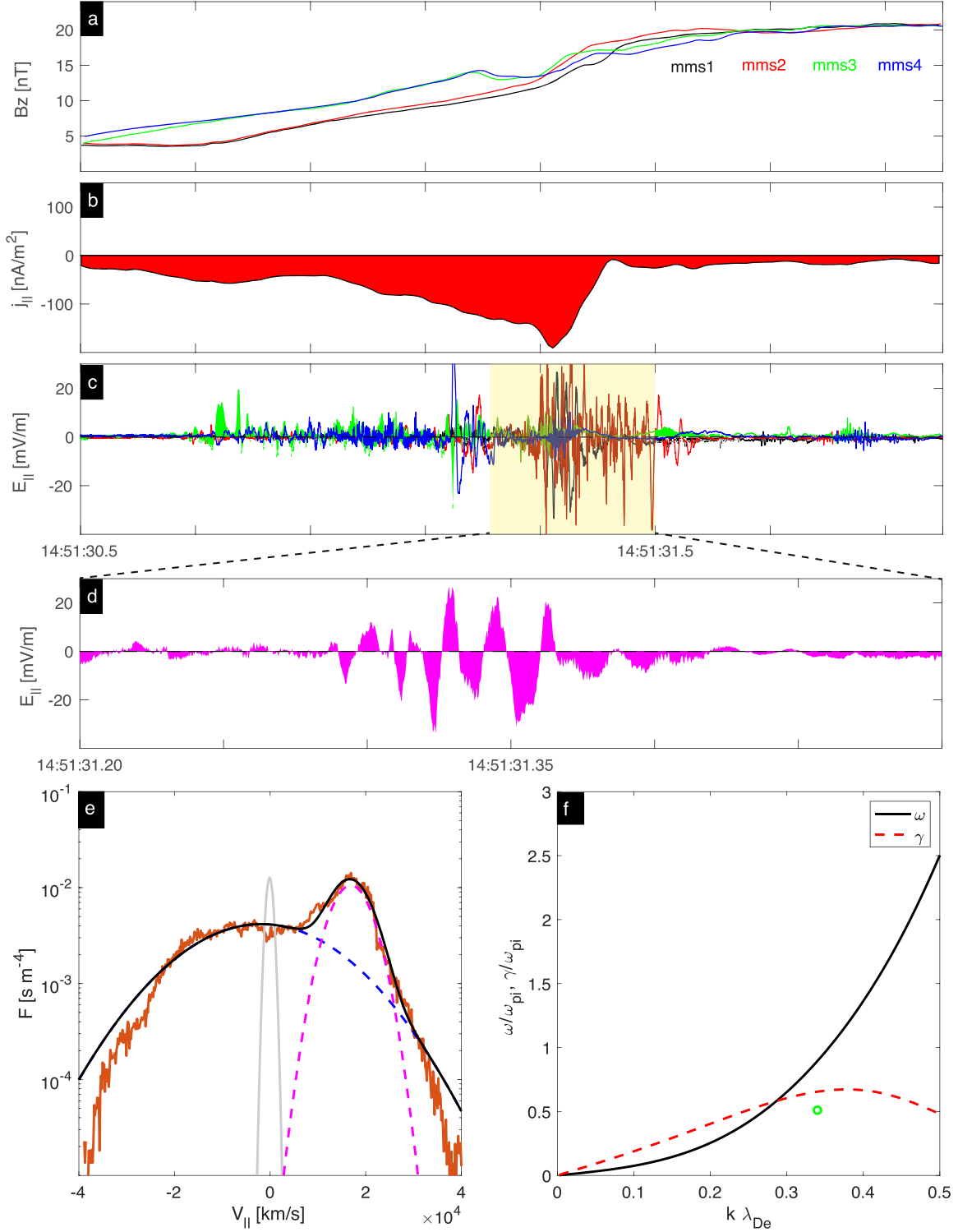


**Figure 4.** Debye-scale electrostatic waves in association with the field-aligned currents: (a) magnetic field  $B_z$  component observed by four MMS spacecraft, (b) field-aligned currents, (c) parallel electric fields observed by four MMS spacecraft, (d) zoomed-in plot of parallel electric field measured by MMS1, (e) Maxwellian fit of electron 1D phase space density in the field-aligned direction: the black line represents electron Maxwellian fit, and the gray line represents ion Maxwellian fit reduced by a factor of 10 for better visibility, and (f) predicted dispersion relation of unstable mode driven by the field-aligned currents. Here the green circle represents the observed wave property.

Khotyaintsev et al. 2016). An imprint is that the electron beam speed stays right below the electron thermal speed. Therefore, the Debye-scale turbulence limits the intensity of the field-aligned currents, coupling back to the larger-scale dynamics.

## 7. Discussions

Using high-cadence data from the MMS mission, we demonstrate that jet braking induces coupling among phenomena from the MHD scale down to the Debye scale, as illustrated

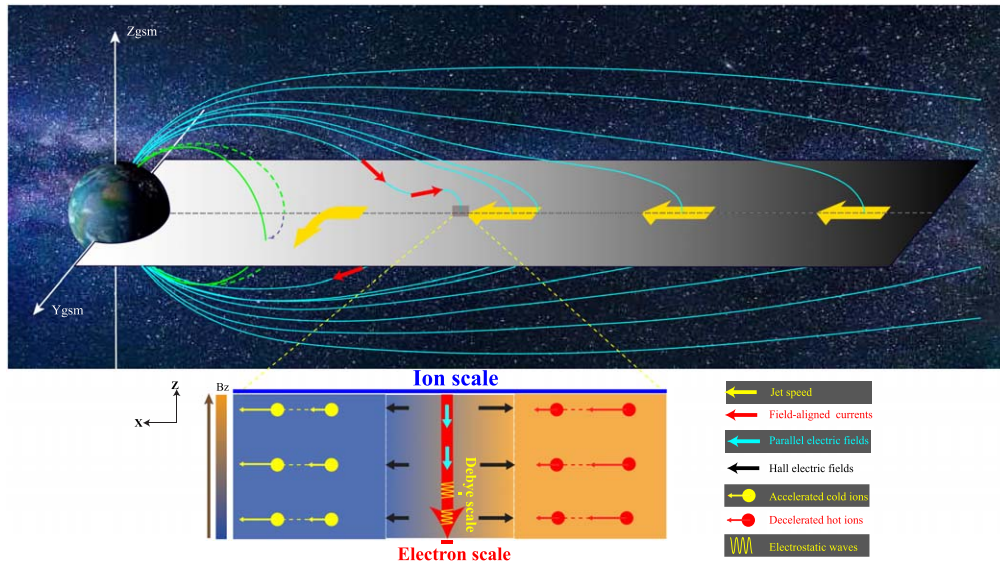


**Figure 5.** Sketch illustrating the cross-scale dynamics driven by plasma jet braking in geospace. MHD-scale jets produced by magnetic reconnection in the mid-tail brake and get diverted in the near-Earth region, leading to distortion of the magnetic field lines and development of an ion-scale DF (shaded rectangular region) hosting strong Hall electric fields that contribute to the local braking of the jet. Parallel electric fields arising from the ion-scale Hall physics generate intense electron-scale field-aligned currents, which drive strong Debye-scale electrostatic waves. Debye-scale turbulence conversely limits the intensity of the field-aligned currents, thereby coupling back to the larger-scale dynamics and mediating the magnetosphere-ionosphere coupling.

in Figure 5. When jets are slowed down and get diverted into the dawn–dusk direction in the near-Earth region, they push nearby magnetic field lines, leading to distortion of the magnetic field line. A clear feature associated with such distortion is the bipolar change of the  $B_Y$  component during neutral sheet crossing, which is seen in our observation and also in recent MHD simulations (e.g., Birn & Hesse 2014; Merkin et al. 2019). The local observation by MMS is a snapshot of such a large-scale process.

Jet braking is confirmed to be connected with the establishment of kinetic-scale structures at the ion-scale jet front. Intense sub-ion-scale Hall electric fields, established in response to the jet evolution, are observed at the front. On the front’s low-density side, an intense tailward Hall field is observed, which has been predicted by recent particle-in-cell simulations (Drake et al. 2014) but never reported in observations hitherto. We find that the intense tailward Hall field can constitute a strong potential difference close to ion thermal energy; therefore, they can reflect and brake the local ion flow.

Sub-ion-scale Hall physics is observed to be related with the formation of the electron-scale electron beam. Recent kinetic analysis (Ganguli et al. 2018) suggests that electrostatic Hall potential arising from Hall fields at the front varies along the magnetic field line since local values of plasma parameters are different. The varying Hall potential along the magnetic field line thus will cause parallel electrostatic potential along the field line and therefore the parallel electric field. The consequent parallel electric field is predicted to peak within the Hall  $E_X$  peak (Ganguli et al. 2018), consistent with our observations where the electron beam and the Hall  $E_X$  peak are simultaneously detected. In our case, the consequent field-aligned currents are intense ( $\sim 400 \text{ nA m}^{-2}$ ), at least an order of magnitude larger than previously reported (e.g., Liu et al. 2013).

The electron-scale beam is found to be further constrained by Debye-scale turbulence. Owing to their slow phase speed, these electrostatic waves can couple the fast electrons to background slow ions, leading to braking of the beam and therefore limiting

the intensity of the field-aligned currents developed at larger scales. Our observations, demonstrating cross-scale dynamics driven by jet braking for the first time, may help in understanding how energy deposited in large-scale structures is transferred to small-scale structures in space.

We greatly appreciate the MMS Science Data Center for providing the data and IRFU-MATLAB for providing analysis codes for this study. This research was supported by NSFC grants 41874188, 41821003, and 42104164.

### ORCID iDs

C. M. Liu <https://orcid.org/0000-0002-9705-5387>  
Y. V. Khotyaintsev <https://orcid.org/0000-0001-5550-3113>  
H. S. Fu <https://orcid.org/0000-0002-4701-7219>  
D. B. Graham <https://orcid.org/0000-0002-1046-746X>  
Y. Y. Liu <https://orcid.org/0000-0002-0765-1709>  
J. L. Burch <https://orcid.org/0000-0003-0452-8403>

### References

- Angelopoulos, V., Runov, A., Zhou, X.-Z., et al. 2013, *Sci*, **341**, 1478  
Akasofu, S.-I. 2015, *PEPS*, **2**, 1  
Birn, J., & Hesse, M. 2014, *JGRA*, **119**, 3503  
Birn, J., Hesse, M., Nakamura, R., & Zaharia, S. 2013, *JGRA*, **118**, 1960  
Burch, J. L., Moore, T. E., Torbert, R. B., et al. 2016, *SSRv*, **199**, 5  
Che, H., Drake, J. F., Swisdak, M., & Yoon, P. H. 2010, *GeoRL*, **37**, L11105  
Deng, X. H., Ashour-Abdalla, M., Zhou, M., et al. 2010, *JGR*, **115**, A09225  
Drake, J. F., Swisdak, M., Cassak, P. A., & Phan, T. D. 2014, *GeoRL*, **41**, 3710  
Ergun, R. E., Goodrich, K. A., Stawarz, J. E., Andersson, L., & Angelopoulos, V. 2014, *JGRA*, **120**, 1832  
Fu, H. S., Cao, J. B., Cully, C. M., et al. 2014, *JGRA*, **119**, 9089  
Fu, H. S., Grigorenko, E. E., Gabrielse, C., et al. 2020, *ScChD*, **63**, 235  
Fu, H. S., Khotyaintsev, Y. V., André, M., et al. 2011, *GeoRL*, **38**, L16104  
Fu, H. S., Khotyaintsev, Y. V., Vaivads, A., et al. 2012a, *GeoRL*, **39**, L06105  
Fu, H. S., Khotyaintsev, Y. V., Vaivads, A., et al. 2012b, *GeoRL*, **39**, L10101  
Fu, H. S., Khotyaintsev, Y. V., Vaivads, A., et al. 2013, *NatPh*, **9**, 426  
Fu, H. S., Vaivads, A., Khotyaintsev, Y. V., et al. 2017, *GeoRL*, **44**, 37  
Ganguli, G., Crabtree, C., Fletcher, A. C., et al. 2018, *NatSR*, **8**, 17186  
Graham, D. B., Khotyaintsev, Y. V., Vaivads, A., & André, M. 2016, *JGRA*, **121**, 3069



- Grigorenko, E. E., Kronberg, E. A., Daly, P. W., et al. 2016, *JGRA*, **121**, 9985
- Huang, S. Y., Fu, H. S., Yuan, Z. G., et al. 2015a, *JGRA*, **120**, 4496
- Huang, S. Y., Jiang, K., Fu, H. S., et al. 2019, *GeoRL*, **46**, 13640
- Huang, S. Y., Sahraoui, F., Retino, A., et al. 2016, *GeoRL*, **43**, 7850
- Huang, S. Y., Wei, Y. Y., Yuan, Z. G., et al. 2020, *ApJ*, **896**, 67
- Huang, S. Y., Yuan, Z. G., Ni, B. B., et al. 2015b, *JASTP*, **129**, 119
- Huang, S. Y., Zhou, M., Deng, X. H., et al. 2012, *AnGeo*, **30**, 97
- Hwang, K.-J., Goldstein, M. L., Vinas, A. F., et al. 2014, *JGRA*, **119**, 2484
- Jiang, K., Huang, S. Y., Yuan, Z. G., et al. 2020, *GeoRL*, **47**, e2020GL088448
- Khotyaintsev, Y. V., Cully, C. M., Vaivads, A., et al. 2011, *PhRvL*, **106**, 165001
- Khotyaintsev, Y. V., Graham, D. B., Norgren, C., et al. 2016, *GeoRL*, **43**, 5571
- Lindqvist, P. A., Olsson, G., Torbert, R. B., et al. 2016, *SSRv*, **199**, 137
- Liu, C. M., & Fu, H. S. 2019, *ApJL*, **873**, L2
- Liu, C. M., Fu, H. S., Liu, Y. Y., et al. 2020, *JGRA*, **125**, e27777
- Liu, C. M., Fu, H. S., Vaivads, A., et al. 2018a, *GeoRL*, **45**, 556
- Liu, C. M., Fu, H. S., Xu, Y., et al. 2018b, *GeoRL*, **45**, 4628
- Liu, C. M., Vaivads, A., Graham, D. B., et al. 2019, *GeoRL*, **46**, 12702
- Liu, J., Angelopoulos, V., Runov, A., & Zhou, X.-Z. 2013, *JGRA*, **118**, 2000
- Lu, S., Angelopoulos, V., & Fu, H. S. 2016, *JGRA*, **121**, 9483
- Merkin, V. G., Panov, E. V., Sorathia, K., & Ukhorskiy, A. Y. J. 2019, *JGRA*, **124**, 8647
- Nakamura, R., Vasani, A., Genestreti, K., et al. 2018, *JGRA*, **123**, 1260
- Norgren, C., André, M., Vaivads, A., & Khotyaintsev, Y. V. 2015, *GeoRL*, **42**, 1654
- Ohtani, S. I., Shay, M. A., & Mukai, T. 2004, *JGR*, **109**, A03210
- Panov, E. V., Nakamura, R., Baumjohann, M., et al. 2010, *GeoRL*, **37**, L08103
- Pollock, C., Moore, T., Jacques, A., et al. 2016, *SSRv*, **199**, 331
- Runov, A., Angelopoulos, V., Sitnov, M. I., et al. 2009, *GeoRL*, **36**, L14106
- Russell, C. T., Anderson, B. J., Baumjohann, W., et al. 2016, *SSRv*, **199**, 189
- Sergeev, V., Angelopoulos, V., Apatenkov, S., et al. 2009, *GeoRL*, **36**, L21105
- Shiokawa, K., Baumjohann, W., & Haerendel, G. 1997, *GeoRL*, **24**, 1179
- Steinvall, K., Khotyaintsev, Y. V., Graham, D. B., et al. 2019, *GeoRL*, **46**, 55
- Sun, W. J., Fu, S. Y., Parks, G. P., et al. 2014, *JGRA*, **119**, 5272
- Torbert, R. B., Burch, J. L., Phan, T. D., et al. 2018, *Sci*, **362**, 1391
- Turner, D. L., Fennell, J. F., Blake, J. B., et al. 2016, *GeoRL*, **43**, 7785
- Vaivads, A., Khotyaintsev, Y. V., André, M., et al. 2004, *PhRvL*, **93**, 105001
- Wei, Y. Y., Huang, S. Y., Yuan, Z. G., et al. 2021, *JGRA*, **126**, e29408
- Wei, Y. Y., Huang, S. Y., Yuan, Z. G., et al. 2022, *JGRA*, **127**, e29761
- Yao, Z. H., Rae, I. J., Guo, R. L., et al. 2017, *JGRA*, **122**, 4335
- Zhou, M., Deng, X. H., Ashour-Abdalla, M., et al. 2013, *JGRA*, **118**, 674
- Zhou, M., Ni, B. B., Huang, S. Y., et al. 2014, *JGRA*, **119**, 4335
- Zhou, X.-Z., Runov, A., Angelopoulos, V., Artemyev, A. V., & Birn, J. 2018, *JGRA*, **123**, 429